journal

J. Am. Ceram. Soc., 77 [7] 1711-18 (1994)

Nucleation and Growth of α′-SiAlON on α-Si_3N_4

Shyh-Lung Hwang† and I-Wei Chen*

Department of Materials Science and Engineering, University of Michigan, Ann Arbor, Michigan 48109-2136

Morphology, composition, and growth defects of α′-SiAlON have been studied in a fine-grained material with an overall composition $Y_{0.33}Si_{10}Al_2O_1N_{15}$ prepared from α-Si_3N_4, AlN, Al_2O_3, and Y_2O_3 powders. TEM analysis has shown that fully grown α′-SiAlON grains always contain an α-Si_3N_4 core, implicating heterogeneous nucleation operating in the present system. The growth mode is epitaxial, despite the composition and lattice parameter difference between α-Si_3N_4 and α′-SiAlON. The inversion boundary that separates two domains in the seed crystal is seen to continue in the grown α′-SiAlON. Lacking a special growth habit, the growth typically proceeds from more than one site on the seed crystal, and the different growth fronts impinge on each other to give an equiaxed appearance of α′-SiAlON. Misfit dislocations on the α/α′ interface are identified as [0001] type (b = 5.62 Å) and 1/3 [1$\bar{2}$10] type (b = 7.75 Å). These nucleation and growth characteristics dictate that microstructural control of α′-SiAlON must rest on the size distribution of the starting α-Si_3N_4 powder.

I. Introduction

THE composition of α′-SiAlON, a solid solution of α-Si_3N_4, can be expressed as $M_{m/z}Si_{12-(m+n)}Al_{m+n}O_nN_{16-n}$, in which M^{z+} is an interstitial cation[1,2] (Li^+, Mg^{2+}, Ca^{2+}, Y^{3+}, and lanthanides except La^{3+} and Ce^{3+},[3-8]). These cations are required for charge compensation during nonstoichiometric substitution of Si by Al and of O by N. Like β-Si_3N_4 and β′-SiAlON, α′-SiAlON is a high-strength ceramic.[9,10] Moreover, its capacity for incorporating a variety of metal ions other than Si and Al, by postdensification annealing affords the possibility of making nitride ceramics of a much lower glass content. Very impressive high-temperature strength has been reported for silicon nitride ceramics containing α′-SiAlON.[11,12]

Much information is already available regarding the formation and the solid-solution range of α′-SiAlON.[3-8] It is generally believed that α′-SiAlON forms by a solution–reprecipitation mechanism from an oxynitride melt, which is a transient reaction product of starting oxide and nitride powders.[9,10] The densification kinetics for α′-SiAlON with Si_3N_4, AlN, Al_2O_3, and Y_2O_3 as starting powders have been delineated recently.[13] In the present work, transmission electron microscopy is used to further elucidate the microscopic aspects of the nucleation and growth processes of α′-SiAlON.

In the course of the present study, several structural defects of α′-SiAlON were identified. The first one is an inversion boundary which separates two domains related by a simple inversion and exists in an α-Si_3N_4 structure because it has no center of symmetry.[14-16] This planar defect is found to exist in α-Si_3N_4 and extends continuously into α′-SiAlON grown onto the α-Si_3N_4 seed. Inversion boundary-like planar defects have been reported in α-Si_3N_4 grains before,[17] but their nature and definitive structural analysis were not established. Another planar defect, identified as the so-called coherent domain boundary, or the δ boundary, was seen between different growth variants of α′-SiAlON. Interface dislocations between α-Si_3N_4 and α′-SiAlON with a Burgers vector along either *a*- or *c*-axis have also been identified. (While dislocations in β-Si_3N_4 are fairly well-known,[18-23] the investigation of dislocations in α-Si_3N_4 or α′-SiAlON is limited.[21]) This information will be used to corroborate our understanding of microstructural development.

II. Experimental Procedure

α′-SiAlON with an overall composition of $Y_{0.33}Si_{10}Al_2O_1N_{15}$ was prepared from α-Si_3N_4, AlN, Al_2O_3, and Y_2O_3 powders. The medium size of α-Si_3N_4 particles was 0.48 μm; 85% of the powders were below 1.0 μm. A detailed description of the powder processing and hot-pressing procedure can be found in Ref. 13, in which the present material was referred to as 1010 composition (corresponding to m = 1.0 and n = 1.0). Full densification was achieved by hot-pressing at 1550°C for 30 min. The as-hot pressed material is superplastic and can be biaxially punch-stretched to larger strains.[24,25] The majority of the specimens examined in this study, however, were given a further annealing at 1600°C for 1 h to slightly coarsen the microstructure. Using X-ray diffraction (XRD) analysis, the lattice parameters of α′-SiAlON were determined. The amount of α′-SiAlON and (unreacted) α-Si_3N_4 was estimated from the peak heights of (10$\bar{1}$2) and (2$\bar{1}\bar{1}$0) reflections. (Overlapping peaks were deconvoluted using FWHM = 0.19° for 2θ.) In addition, an α′ + β′-SiAlON with an overall composition of $Y_{0.2}Si_{10.4}Al_{1.6}O_1N_{15}$ (material 0610 in Ref. 13) was examined to compare the morphology of α′-SiAlON grains in different phase assemblages. The preparation of this material followed a procedure similar to the above.

Foils for transmission electron microscopy (TEM) were prepared from slices cut from the annealed material. The slices were hand-ground to less than 30 μm thick, followed by polishing, dimpling, and ion milling. A thin layer of carbon was evaporated onto these foils to avoid surface charging under the electron beam.

Microscopy was performed using a scanning electron microscope (SEM, Hitachi S-800, Tokyo, Japan) and an analytical transmission electron microscope (TEM, JEOL 2000FX, Tokyo, Japan) equipped with a thin-window energy-dispersive X-ray analysis (EDS, Tracor-Northern, Middleton, WI) system. Dislocations were analyzed using the conventional **g**·**b** criterion, where **g** is the operating reflection and **b** the Burgers vector.[26] At least two nonparallel reflections that rendered the dislocation out of contrast were used to establish the Burgers vector. To eliminate the interference from both the Moiré fringes and the overlapping strain field in a dislocation array, weak-beam (WB) dark-field (DF) imaging was used.[27] Diffraction patterns were indexed with the help of computer software (Diffract II, Vol. 1.2, Microdev Software, Evergreen, CO).

T. E. Mitchell—contributing editor

Manuscript No. 194678. Received April 20, 1993; approved February 11, 1994.
Supported by the National Science Foundation under Grant No. DDM 9024975.
*Member, American Ceramic Society.
†Now at Oak Ridge National Laboratory, Metals and Ceramics Division, Oak Ridge, TN.

III. Results

(1) General Microstructure

Figure 1 is an SEM micrograph showing the general microstructure of materal 1010 after hot-pressing. Measurement of the grain sizes found a distribution between 0.2 and 0.5 μm. Phase analysis by XRD indicated a phase assemblage of 56% α′-SiAlON and 44% α-Si_3N_4. Evidence to be presented in the following further suggests that the smaller grains are unreacted α-Si_3N_4, and the larger grains are α′-SiAlON containing an α-Si_3N_4 core.

The microstructure after annealing is shown in the TEM micrograph of Fig. 2. It also consists of many large grains embedded in a small-grain matrix. Both large and small grains have an equiaxed grain shape. The average size of the large grains is around 1 μm, which is about three times larger than that of the small grains. Large grains with a size up to 3 μm were often found. Phase analysis by XRD indicated that after annealing, α′-SiAlON comprised 90% of the phase assemblage, the balance being α-Si_3N_4.

We examined a large number of grains (about 50%) within the field of view under TEM. The large grains were found to always contain a core with a contrast different from that of the surrounding shell under bright-field (BF) imaging conditions. Several such core-containing large grains, where the core is marked as α and the shell α′, can be seen in Fig. 2. The boundary between the core and the shell has a strong contrast, a feature consistent with the presence of misfit strain fields in the lattice. The size of the core is about 0.3 μm, which is somewhat smaller than the size of the starting α-Si_3N_4 powders.

Selected area diffraction (SAD) patterns show that the core and the shell have the same α-Si_3N_4 structure and crystallographic orientation (Fig. 2 inset). The interface between the core and the shell is coherent, as revealed by the continuity of the lattice planes across the interface. For example, continuous $(10\bar{1}0)$ lattice planes are shown in Fig. 3. (We have indicated the position of the interface with arrows.) The interface shows no distinct feature in this image, because it is coherent but not edge-on. Despite their structural similarity, the core and shell compositions are different according to EDS. Figure 4 shows that the core contains only Si and N, while the shell contains Al, Y, and O in addition to Si and N. (Due to the small core size and the possible drift of the foil position during data collection, it was usually difficult to completely avoid the signal contribution from the adjacent grains. We could, however, find some cores for which the shell had been removed during thinning the specimen. They provided the best examples where shell contribution was largely avoided. More generally, we could only see a much lower Al, Y, and O content from the core spectra compared to those from the shell spectra. The detection limit for Al and O in our instrument is about 1.5 wt%.) These findings provide a ready explanation for the lighter contrast (Fig. 2) of the core, which lacks the strong, electron-scattering Y. They also identify the core as α-Si_3N_4 and the shell as α′-SiAlON.

Some smaller grains also have a core–shell structure. Others, which contain no core, were sometimes found to have Al, Y, and O. These α′-SiAlON grains may have directly formed without the assistance of a core. On the other hand, if one assumes a slice 0.3 μm thick as representative of the specimen viewed under the TEM, then the probability of sectioning through the shell region (1 μm) without including any part of the core (0.3 μm) is approximately 40%. Taking into account this possibility, it becomes reasonable to suggest that, most likely, every α′-SiAlON grain does contain one α-Si_3N_4 core.

The core–shell structure of α′-SiAlON was also observed in material 0610. After hot-pressing and annealing, this material contained α′ and β′-SiAlON in approximately equal fractions, with some residual α-Si_3N_4. Figure 5 shows the microstructure after annealing. It contains both elongated β′-SiAlON grains

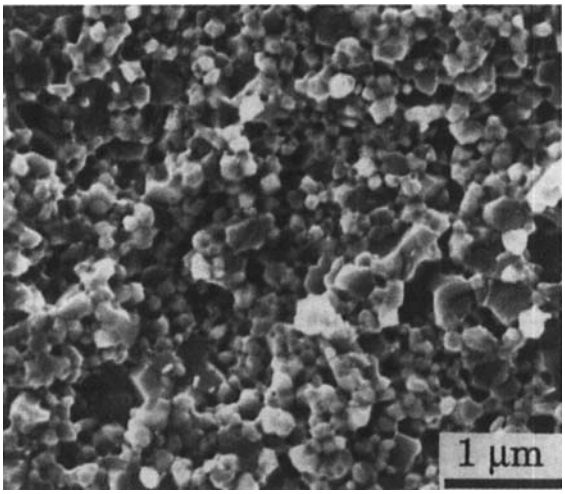

Fig. 1. SEM micrograph of material 1010 after hot-pressing at 1550°C.

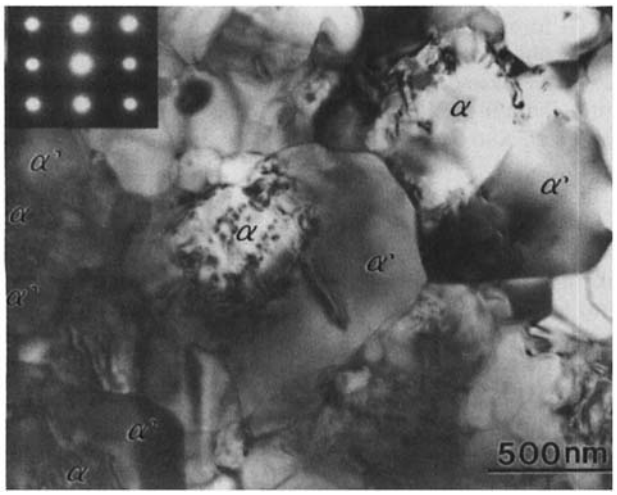

Fig. 2. BF image showing α′-SiAlON grains with α-Si_3N_4 core. The dislocation contrast between α/α′ can be clearly observed. The diffraction pattern of the α/α′ region is shown in the inset (B = $[11\bar{2}0]$).

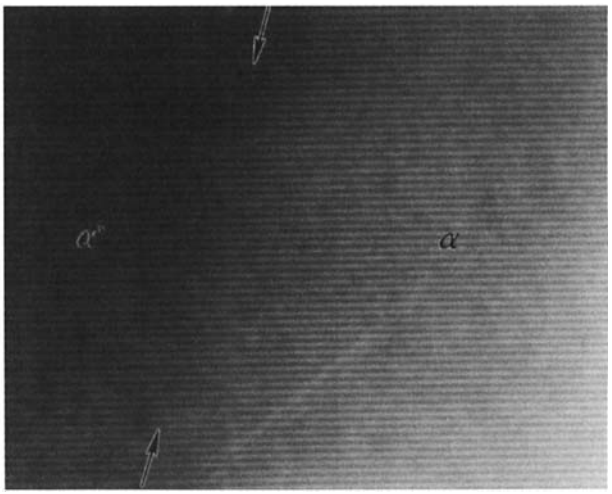

Fig. 3. $\{10\bar{1}0\}$ lattice image of the interface between α-Si_3N_4 core and α′-SiAlON shell showing the continuity of the lattice planes across the interface. (The contrast difference is due to the compositional difference.)

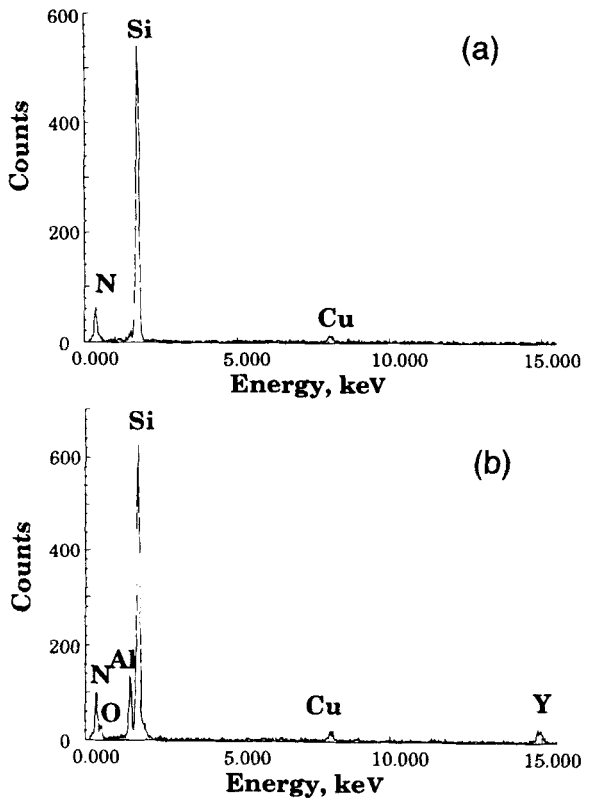

Fig. 4. EDS spectra taken from (a) α-Si_3N_4 core and (b) α′-SiAlON shell. The core contains no Al, O, or Y, and hence is α-Si_3N_4. (Cu from supporting grid.)

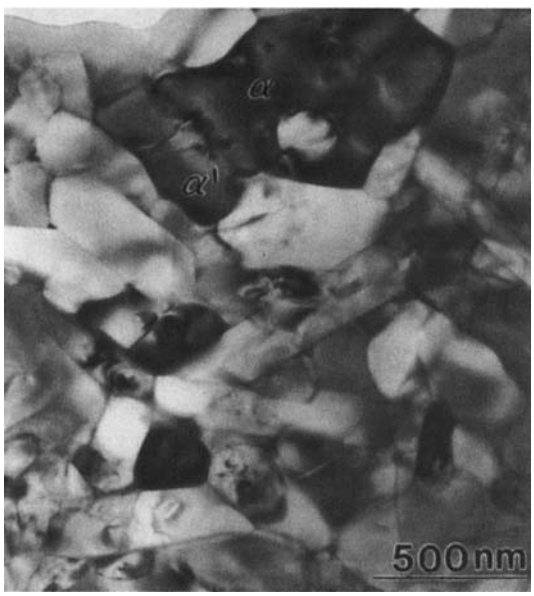

Fig. 5. BF image showing both elongated β′-grains and an equiaxed α′-SiAlON-grain with a core/shell structure. (Material 0610.)

and equiaxed α′-SiAlON grains. The α′-SiAlON grain marked in Fig. 5 again has a core–shell microstructure rather similar in size and proportion to those in material 1010.

(2) Interface Dislocations

Misfit strains exist at the interface due to the compositional difference between the α-Si_3N_4 core and the α′-SiAlON shell. This misfit gives rise to two features. First, Moiré fringes can be seen under appropriate BF diffraction conditions (Fig. 6(a)). Second, interface dislocations can be seen under WB imaging conditions. One example is shown in Fig. 6(b) for $\mathbf{g} = 02\bar{2}\bar{1}$.

These dislocations form a network of two arrays, which are better revealed in Figs. 7(a) and (b). Contrast analysis shows that one set of these dislocations is out of contrast under $\bar{2}3\bar{1}0$, $1\bar{3}20$, $1\bar{2}10$, and $1\bar{1}00$ diffraction conditions but in strong contrast under a 0004 diffraction condition (Fig. 7(a)). Therefore, they have a [0001] Burgers vector; i.e., they are *c*-axis dislocations. Their edge character is evident from the line direction in Fig. 7(a), which is mostly perpendicular to 0004. The other set of dislocations, which is out of contrast under 0004 and $10\bar{1}2$ diffraction conditions, is in strong contrast under $\bar{2}3\bar{1}0$ diffraction condition (Fig. 7(b)). They probably have a $1/3[1\bar{2}10]$ Burgers vector, which is the shortest perfect dislocation Burgers vector in an α-Si_3N_4 structure, and possess an edge character as well. For the $2\bar{2}01$, $02\bar{2}\bar{1}$, $1\bar{3}2\bar{1}$, and $3\bar{5}21$ diffraction conditions, both sets of dislocations are in contrast (Fig. 6(b) for $02\bar{2}\bar{1}$). This is consistent with the [0001] and $1/3[1\bar{2}10]$ designations for the Burgers vectors.

From the average spacing of Moiré fringes and interface dislocations, the differences in the lattice parameters between the α-Si_3N_4 core and α′-SiAlON shell can be estimated. The average spacing of Moiré fringes for 0002 reflection is 135 Å, which corresponds to a difference of 0.059 Å in the lattice parameters along the *c*-axis. The average spacing of [0001] and $1/3[1\bar{2}10]$ dislocations in Figs. 7(a) and (b) are about 460 and 880 Å, respectively. The calculated misfits are 0.069 Å along the *c*-axis and 0.068 Å along the *a*-axis. (The Burgers vector of [0001] and $1/3[1\bar{2}10]$ dislocations are, respectively, 5.62 and 7.75 Å.)[14–16] According to XRD, the lattice misfits are 0.069 Å along the *c*-axis and 0.061 Å along the *a*-axis at room temperature. The reasonable agreement of these data suggests that most of the interfacial strain energy has been relieved by forming the dislocation network.

The micrographs of Figs. 7(a) and (b) contain nodes at dislocation intersections. This could be due to the reaction of two dislocations into, say, a $1/3[1\bar{2}13]$ dislocation. The dislocation interaction is probably also responsible for the wavy configuration in the dislocation arrays. These aspects, however, were not investigated further.

(3) Inversion Boundary

Two types of planar defects, inversion boundary and δ boundary, have been found in the α/α′ core–shell structure. Their configurations are schematically drawn in Fig. 8. We will describe the inversion boundary first and leave the δ boundary to the next section.

An inversion boundary is shown in Fig. 9(a). It appears as a ribbonlike feature winding from the center of the core toward the outer shell. Both ends of the "ribbon" have sliced across the α/α′ interface to reach the shell (see arrows in Fig. 9(a)). These planar defects do not usually show any fringe image contrast except under the WB DF imaging conditions. This is probably due to the large extinction distance of this material, which, at the minimum, is about 1000 Å for, say, the (0004) reflection.[29] Trace analysis determines that these defects lie primarily on (0001) planes, but they frequently change from one (0001) plane to another by going through some irrational planes in between. This can also be seen in Fig. 9(a). The regions separated by these planar defects show no contrast difference in any BF imaging conditions (Figs. 9(a–b)), indicating identical crystallographic orientation.

As mentioned in the Introduction, the α-Si_3N_4 structure can have two inversion domains related by a simple inversion. Their impingement results in an inversion boundary, across which a contrast difference arises under DF imaging conditions when Friedel's law is violated.[30] According to Serneels *et al.*[31] and Biest and Thomas,[30] an inversion boundary shows no contrast under any BF imaging conditions but gives a strong contrast under certain multiple-beam conditions in which the

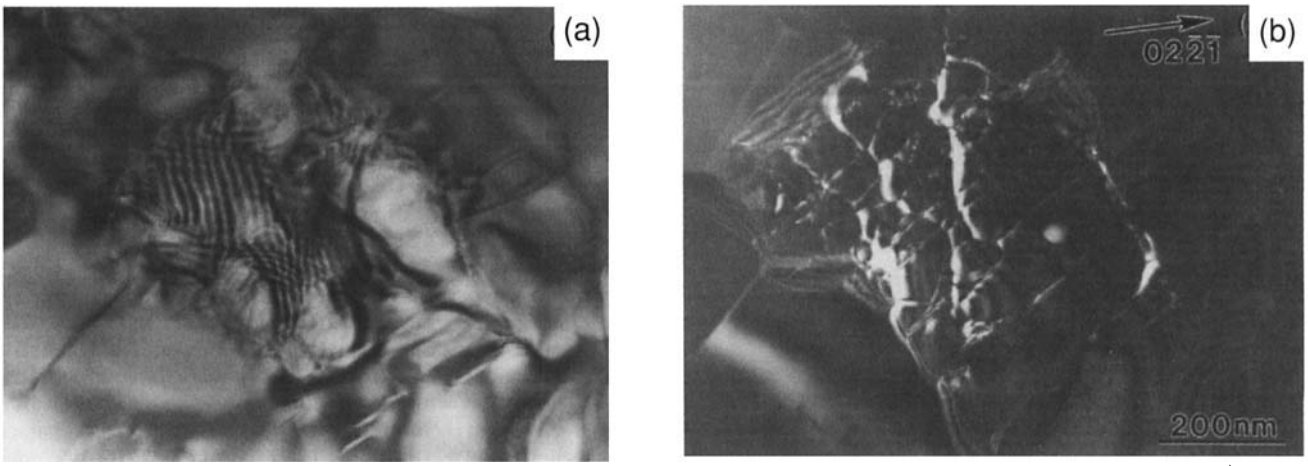

Fig. 6. TEM micrographs of an α/α' interface showing (a) Moiré fringes under BF condition and (b) interfacial dislocation network under WB condition.

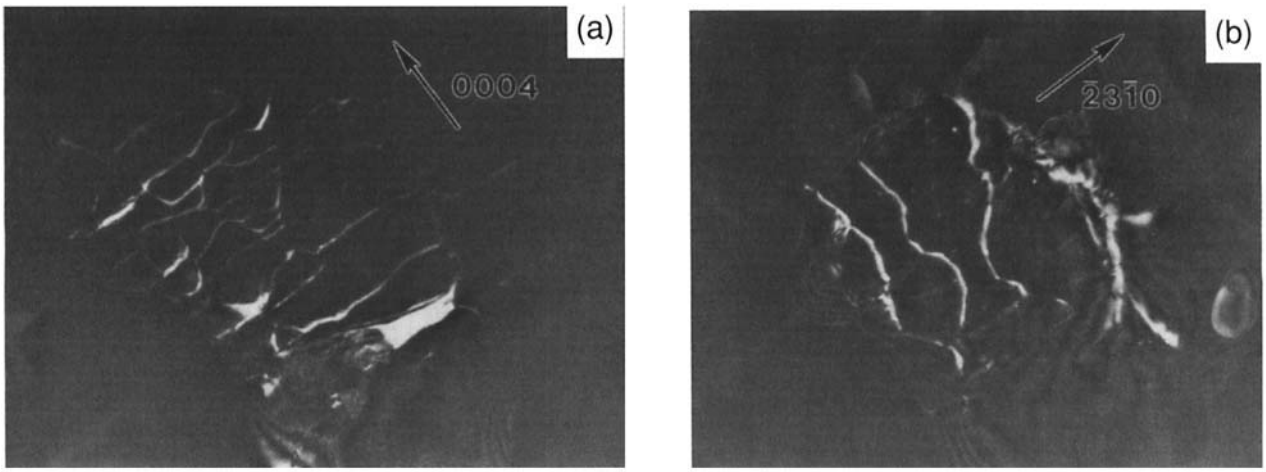

Fig. 7. WB images of dislocations at α/α' interface with Burgers vector of (a) [0001] and (b) 1/3 $[1\bar{2}10]$. The [0001] dislocations are visible when $\mathbf{g} = 0004$ and the 1/3 $[1\bar{2}10]$ dislocations are visible when $\mathbf{g} = \bar{2}3\bar{1}0$.

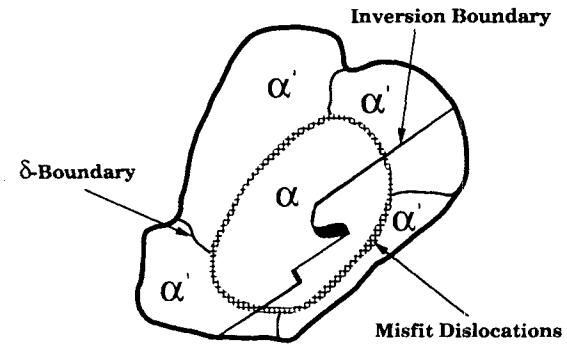

Fig. 8. Growth morphology of α'-SiAlON on α-Si_3N_4 showing inversion boundary, δ boundaries, and misfit dislocations.

crystal projection lacks a center of symmetry. This latter condition is satisfied by $B \approx [1\bar{2}10]$ and $\mathbf{g} = \bar{1}011$, as in Fig. 9(c), where the boundary is visible and a strong contrast across the interface arises in the DF image.

Additional diffraction contrast analysis on this boundary under two-beam conditions, using the structural model to be discussed in Section IV(3), was also performed. Table I summarizes the calculated structure factors, the phase angle differences, and the observed image contrast for 10 diffraction conditions. When the phase angle difference between two regions is close to zero, the boundaries are virtually invisible. This is the case in Fig. 9(b), for example, for the 0004 diffraction condition. (The two features marked by arrows in Fig. 9(b) are cracks which formed *in situ* after long exposure to an electron beam.) When the phase angle difference is not zero, a strong contrast for the boundary is always found, even though the two separated regions show no contrast difference, as in Fig. 9(a) for the $10\bar{1}0$ diffraction condition. Thus, the structural model described in Section IV(3) and the conclusion that the boundary is an inversion boundary are verified.

The inversion boundary described above was most likely inherited from the starting α-Si_3N_4. Since the growth of α'-SiAlON onto the α-Si_3N_4 core is obviously epitaxial, these defects are carried over into the α'-SiAlON shell, which has the same space group as α-Si_3N_4. Indeed, the continuation of the inversion boundary across the α/α' interface provides additional evidence for epitaxial growth. The frequency of the occurrence of the inversion boundaries, however, is quite low. This could indicate that the interfacial energy of the inversion

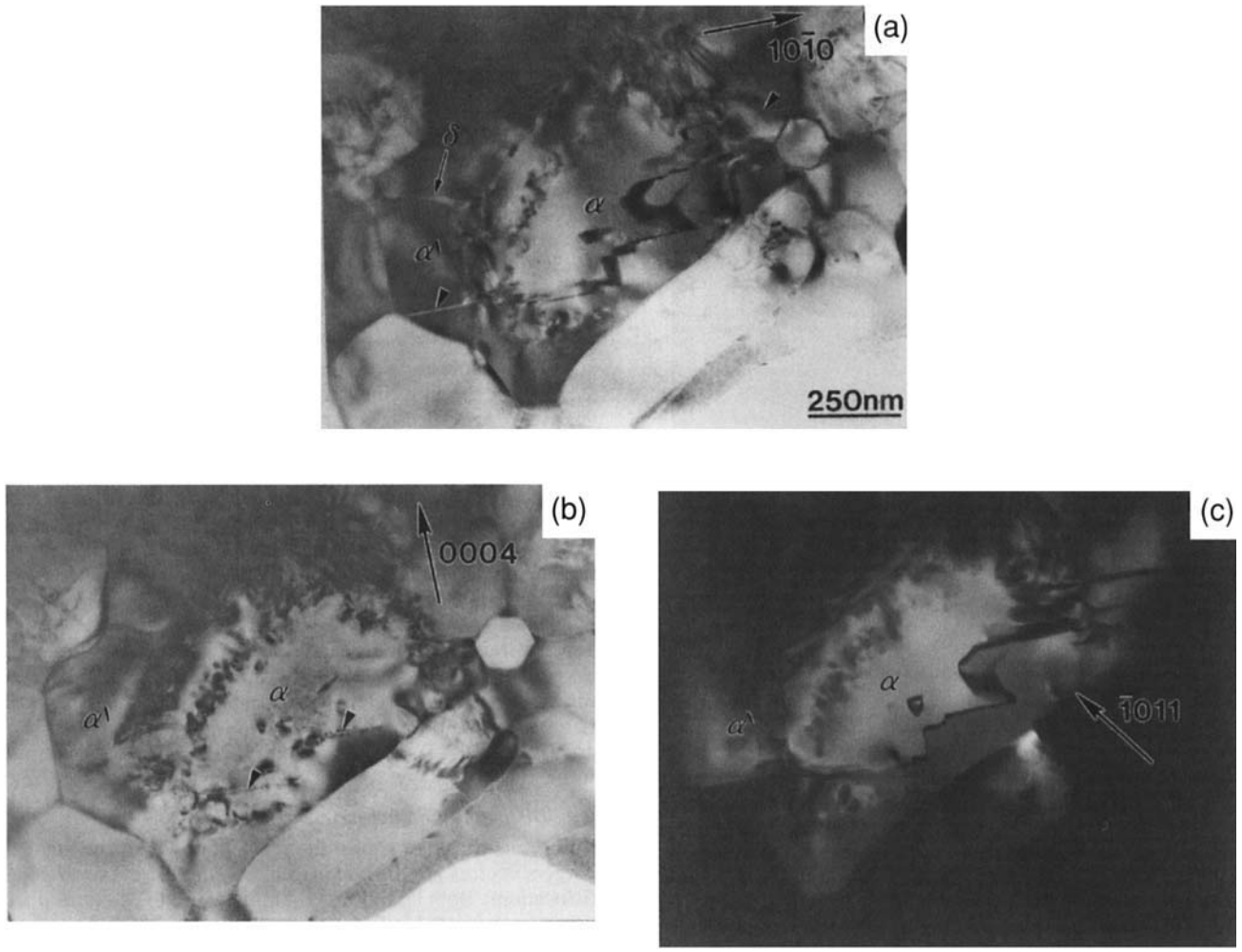

Fig. 9. BF micrographs showing the inversion boundary and its continuity into the shell region. The boundary is (a) visible when $\mathbf{g} = 10\bar{1}0$ and (b) invisible when $\mathbf{g} = 0004$. The portions of boundary in the shell region are marked by arrows in (a). The electron-beam-induced microcracks are marked by arrows in (b). (c) DF image showing strong contrast difference between inversion domains. $B \approx [1\bar{2}10]$, $g = \bar{1}011$.

Table I. Structure Factor, Phase Angle Difference, and Contrast Analysis of Inversion Boundary

Diffraction condition	Structure factor	Phase angle difference	Visibility
$10\bar{1}0$	7.74	120	Visible
$\bar{1}101$	15.79	180	Visible
$0\bar{1}1\bar{1}$	15.85	60	Visible
$\bar{1}011$	15.87	60	Visible
$\bar{2}02\bar{1}$	14.84	120	Visible
0004	39.12	0	Invisible
$20\bar{2}1$	14.80	1.5	Invisible
$30\bar{3}1$	16.83	0.3	Invisible
$30\bar{3}\bar{1}$	16.75	0.1	Invisible
$\bar{2}24\bar{2}$	21.32	0.4	Invisible

boundaries in the starting powder may be quite high. Indeed, the unusual occurrence of beam-induced cracking at these boundaries implies a relatively low cohesive energy which would be consistent with a relatively high boundary energy.

(4) δ Boundary (Coherent Domain Boundary)

The inversion boundries discussed above have a well-defined crystallographic plane and are continuous across the α/α′ interface. We have also observed another type of planar defect which does not lie on any well-defined crystallographic plane and which exists in the α-SiAlON shell only. One such defect is already visible in Fig. 9(a) and is marked as δ. It ends at the α/α′ interface but spans across the entire α′ shell. This latter feature is characteristic of such planar defects. For example, Fig. 10 shows several δ boundaries all terminating at the α/α′ interface.

Essentially, no crystallographic difference can be observed under any diffraction conditions between neighboring α′-SiAlON regions separated by δ boundaries. According to Gever *et al.*,[32] a fringe contrast can still arise from a very small misorientation between the simultaneously excited reflections of the two neighboring growth variants. Such boundaries have been termed δ boundaries or coherent domain boundaries in the literature. In our case, it seems plausible that the number of coherent domain boundaries coincides with the number of α′-SiAlON nuclei grown from a single α-Si_3N_4 core.

Lastly, since α′-SiAlON can also exhibit inversion domains, it can nucleate on the α-Si_3N_4 in either of the two inverted domains. This possibility could exist independently of whether there is a domain boundary in the substrate (much like SiC or GaAs growing on Si). If so, the above "δ-boundaries" could actually be inversion boundaries and the domains should have the same contrast. (They look as though they do in the micrographs.) This point, however, was not pursued further in our study. The important point regarding intergrowth kinetics, though, still stands; namely, the number of domain boundaries in the α′-SiAlON shell most likely coincides with the number of α′-SiAlON nuclei grown from a single α-Si_3N_4 core.

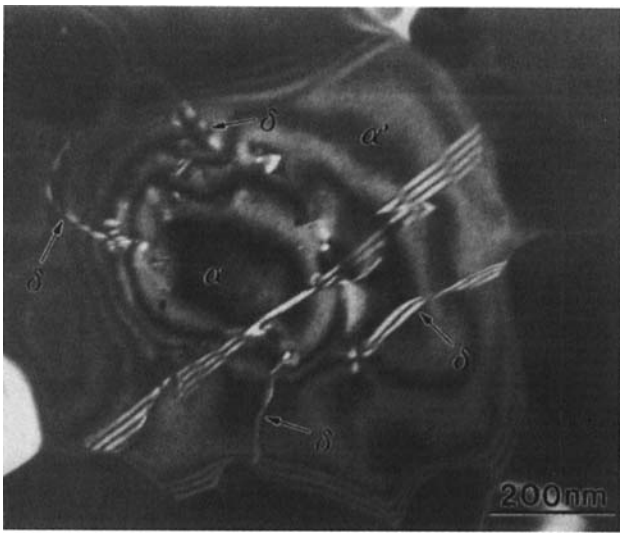

Fig. 10. WB image showing growth variants of α′-SiAlON from a single α-Si_3N_4. The δ boundary between neighboring variants is marked by arrows.

IV. Discussion

(1) Formation Mechanism of α′-SiAlON

As shown in our recent study of hot-pressing kinetics using α-Si_3N_4, AlN, Al_2O_3, and Y_2O_3 powders,[13] the metal oxides first react with residual SiO_2 on Si_3N_4 surfaces to form a eutectic melt and $Y_3Al_5O_{12}$. AlN, and later Si_3N_4, then dissolve into the oxide melt and reprecipitate into SiAlON grains. Densification is achieved soon after partial Si_3N_4 dissolution, leaving a large amount of unreacted α-Si_3N_4.

The microstructural observations in the present study indicate that the reprecipitation process proceeds by heterogeneous nucleation of α′-SiAlON onto the remaining α-Si_3N_4 particles, which are somewhat smaller than the starting α-Si_3N_4 particles because of partial dissolution. About 50% of the large grains that were in the field of view of TEM were examined, and all of them contained cores. Such preponderance of evidence of α-Si_3N_4 seeding, at least for the early stage of reprecipitation leading to larger grains, argues for heterogeneous nucleation even if homogeneous nucleation cannot be entirely ruled out. Indeed, with the presence of ample α-Si_3N_4 seeds and with the relative ease of heterogeneous nucleation, the higher supersaturation level required for homogeneous nucleation would be difficult to establish.

There appears to be no preferential nucleation sites on the surface of the α-Si_3N_4 particles, nor is there any special growth habit. This is obvious from the observation of several growth habits (separated by δ boundaries) around a single α-Si_3N_4 particle. Energetically, this may be justified by (a) the small difference in the lattice misfit strain along the *c*-axis (1.2%) and *a*-axis (0.9%), which are both small, and (b) the small energy difference (see below) between *c*-axis and *a*-axis dislocations required for accommodating misfits. In addition, α-Si_3N_4 lacks any special growth direction which can be rationalized by the chemical bonding considerations.[24] Together, these nucleation and growth conditions dictate that microstructural control of α′-SiAlON must rest on the powder characteristics—mean particle size and size distribution—of the starting α-Si_3N_4.

Note that the lattice parameter differences measured in this investigation are higher than those reported in the literature,[28] which are 0.057 and 0.054 Å, respectively, for *a*- and *c*-axis, for the nominal composition $Y_{0.33}Si_{10}Al_2O_1N_{15}$ on α-Si_3N_4. This indicates that the solute contents in the α′-SiAlON shell in this study are higher than the nominal concentrations. This is possible because some α-Si_3N_4 grains are still trapped inside the α′-SiAlON shell and have not been homogenized. Consequently, the α′-SiAlON formed should be richer in Al, Y, and O, and therefore have larger lattice parameters. Also note that the coexistence of α-Si_3N_4 core and α′-SiAlON shell in the microstructure does not necessarily imply phase equilibrium. Slow solid-state diffusion is deemed common in the silicon nitride system and could have prevented homogenization once the core is cut off from the liquid phase by the surrounding α′-SiAlON shell during processing.

An additional point regarding kinetics and the generality of the observations reported here is the processing condition. In our experience, the feature of core–shell structure was ubiquitously observed in a large variety of Y-containing SiAlON of both single-phase α′ compositions and two-phase α′–β′ compositions.[24] In contrast, such features have only rarely been observed by investigators in the past and received little attention.[33] Direct observations of nucleation sites, here identified as α-Si_3N_4 for the first time, were made possible because of the relatively low processing temperature (1550°C) and short densification time (0.5 h) used in our study. Such processing conditions preserved the early transient evolutions of the silicon nitride system and provided a very large number of fine grains offering favorable sampling statistics for TEM observations. In other studies of silicon nitride ceramics, however, higher processing temperatures were typically used, and the kinetics were so fast that early nucleation events would have been overtaken, and hence obliterated, by later growth and grain coarsening steps. (Grain coarsening and the attendant dissolution and reprecipitation processes would destroy many grains that contain first-generation nuclei.) Thus, despite the fact that this is the first systematic observation of α-Si_3N_4 core/α′-SiAlON shell structure, we suggest that such configurations are very common during the early stage of α′-SiAlON formation.

(2) Dislocation Structure

In the α-Si_3N_4 structure, the dislocations with the smallest Burgers vectors are the *c*-axis (5.62 Å) and the *a*-axis (7.75 Å) dislocations. Both are observed in this work. (The *c*-axis dislocation was reported in Ref. 21; the *a*-axis dislocation is reported here for the first time.) In comparison, in β-Si_3N_4, *c*-axis dislocations have been commonly observed,[18–22] but *a*-axis dislocations (1/3[11$\bar{2}$0]) and some mixed dislocations (1/3[11$\bar{2}$3]) were rarely reported.[20,22] This is understandable because in β-Si_3N_4 the *c*-axis Burgers vector is only 2.91 Å, while the *a*-axis Burgers vector is 7.61 Å, making the *a*-axis dislocation energetically unfavorable. This is not the case for α-Si_3N_4. Indeed, since the number of broken Si–N bonds in an *a*-axis edge dislocation (0.77 $Å^{-1}$) is smaller than that in a *c*-axis edge dislocation (0.89 $Å^{-1}$), the core energy should partially compensate for the difference in the elastic energy. It seems then that in an α-Si_3N_4 structure, *a*- and *c*-axis dislocations should have similar line energy and be able to generate at similar frequencies. This is in agreement with our observations.

With the proper combinations of the two types of dislocations, any strain misfit at the interface between the α-Si_3N_4 core and the α′-SiAlON shell can be largely relieved. This will facilitate nucleation of epitaxial α′-SiAlON at essentially any surface sites on α-Si_3N_4. This is partly responsible for the multiple growth variants and the equiaxed grain shape we observed. Meanwhile, since the *c*-axis dislocation in α-Si_3N_4 has a much larger Burgers vector than the *c*-axis dislocation (that is predominant) in β-Si_3N_4, a higher hardness and a lower fracture energy of α-Si_3N_4 than those of β-Si_3N_4[9,10] are expected.

(3) Inversion Boundary

The impingement of two inversion domains of α-Si_3N_4 results in an inversion boundary. In a Si_3N_4 structure, the Si is tetrahedrally coordinated by four N atoms, while N is triangularly coordinated by three Si atoms. Ideally, across the interface between two inversion domains, these bonding requirements should be fulfilled to minimize the interfacial energy.

The atomic arrangements of the four stacking layers forming an α-Si_3N_4 structure are plotted in Fig. 11, and the coordinates of the atoms are listed in Table II. The reference axes used here

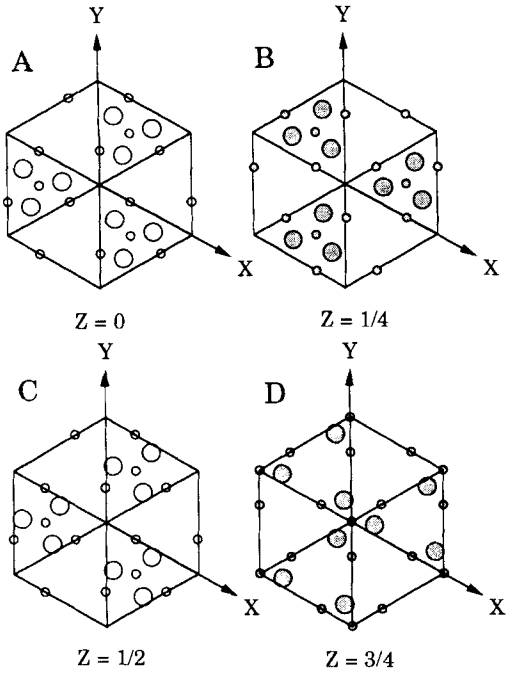

Fig. 11. Atomic arrangements of α-Si_3N_4 structure on four successive layers. Si is represented by large circles and N by small circles.

Table II. Atomic Coordinates in α-Si_3N_4 Structure

	Coordinate
N(1)	(1/3, 2/3, 1/2)(1/3, 2/3, 0)
N(2)	(2/3, 1/3, 1/4)(0, 0, 3/4)
N(3)	(2/3, 2/3, 1/2)(1/3, 0, 1/2) (0, 1/3, 1/2)(1/3, 0, 0) (2/3, 2/3, 0)(0, 1/3, 0)
N(4)	(2/3, 0, 3/4)(0, 2/3, 3/4) (1/3, 1/3, 3/4)(2/3, 0, 1/4) (1/3, 1/3, 1/4)(0, 2/3, 1/4)
Si(1)	(0.833, 0.75, 3/4)(0.25, 0.083, 3/4) (0.917, 0.167, 3/4)(0.417, 0.167, 1/4) (0.75, 0.583, 1/4)(0.833, 0.25, 1/4)
Si(2)	(0.5, 0.917, 1/2)(0.083, 0.583, 1/2) (0.417, 0.5, 1/2)(0.583, 0.833, 0) (0.25, 0.417, 0)(0.167, 0.75, 0)

are different from that in the International Table for X-ray Analysis in that the origin has been shifted from the 31*c* position to the 3-fold axis to make the description of the inversion operation easier. By inspection, it can be easily established that the *x*- and *y*-coordinates of the atoms at $z = 0$ and $z = 1/4$ are related to each other by an inversion operation through the origin. This observation already provides a clue as to why the (0001) plane should be the habit plane between two inversion domains. As shown in Fig. 12(a), the normal α-Si_3N_4 structure with the stacking sequence of A-B-C-D is converted into its inverted form with the stacking sequence D′-C′-B′-A′. Because the atomic arrangement of the A′(B′) layer is similar to that of B(A) layer, the easiest way to maintain the bonding requirements is to form the interface between A/A′ or B/B′ layers. In this way, the stacking sequence across the interface becomes C-D-A-A′-D′-C′ (see Fig. 12(b)), and all the Si–N bonds across the interface are maintained. (The configurations of the next-nearest-neighbor bonds have to be changed, but this is relatively unimportant as far as energy is concerned.) In comparison, interfaces other than (0001) are not energetically favorable, because they must entail relaxation of some Si positions in

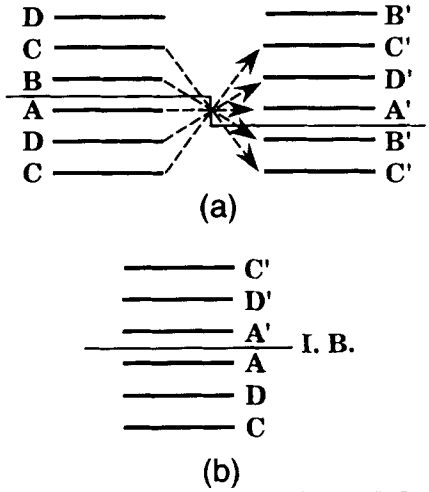

Fig. 12. (a) Inversion operation changing A-B-C-D stacking sequence into A′-D′-C′-B′. (b) Inversion boundary (I.B.) on (0001) plane.

order to maintain Si–N bonding continuity across the interface.[24] This provides a ready explanation for the observed (0001) habit plane for the inversion boundary.

V. Conclusions

(1) Fully grown α′-SiAlON grains always contain an α-Si_3N_4 core, evidence that heterogeneous nucleation operates in the present system.

(2) The growth mode of α′-SiAlON on α-Si_3N_4 is epitaxial despite a compositional difference (in Al, Y, and O) and a lattice parameter difference (around 1% in both *a* and *c* directions) between the two phases.

(3) Inversion boundaries have been observed in α-Si_3N_4 and α′-SiAlON. They originate from the α-Si_3N_4 core and continue across the α/α′ interface into α′-SiAlON, providing further evidence of epitaxial growth of α′-SiAlON on α-Si_3N_4.

(4) The growth typically proceeds from more than one site on the seed crystal, and the growth fronts impinge on each other with an irregular interface (coherent domain boundary or δ boundary). No special growth habit dominates, and the resulting α′-SiAlON grains are equiaxed.

(5) Interface dislocations which accommodate the lattice misfit between α′-SiAlON and α-Si_3N_4 have been identified as [0001] type and 1/3 [$1\bar{2}10$] type.

(6) Given the above nucleation and growth characteristics, the microstructural control of α′-SiAlON is believed to rest on the size distribution of the starting α-Si_3N_4 powder.

Acknowledgment: We are grateful for the illuminating comments of the associate editor on the crystallographic nature of inversion and δ boundaries.

References

[1]S. Hampshire, H. K. Park, and D. P. Thompson, "α′-SiAlON Ceramics," *Nature (London)*, **274** [5674] 880–82 (1978).

[2]H. K. Park, D. P. Thompson, and K. H. Jack, "α′-SiAlON Ceramics"; pp. 251–56 in *Science of Ceramics 10*. Edited by H. Hausner. Deutsche Keramische Gesellschaft, Cologne, Germany, 1980.

[3]Z.-K. Hwang, P. Greil, and G. Petzow, "Formation of α-Si_3N_4 Solid Solutions in the System Si_3N_4-AlN-Y_2O_3," *J. Am. Ceram. Soc.*, **66** [6] C-96–C-97 (1983).

[4]Z.-K. Hwang, T.-Y. Tien, and T.-S. Yen, "Subsolidus Phase Relationships in Si_3N_4-AlN-Rare-Earth Oxide Systems," *J. Am. Ceram. Soc.*, **69** [10] C-241–C-242 (1986).

[5]S. F. Kuang, Z. K. Hwang, W. Y. Sun, and T.-S. Yen, "Phase Relationships in the Li_2O-Si_3N_4-AlN System and the Formation of Lithium-α′-SiAlON," *J. Mater. Sci.*, **25**, 72–74 (1990).

[6]G. Grand, J. Demit, J. Ruster, and J. P. Torre, "Composition and Stability of Y-Si-Al-O-N Solid Solutions Based on α-Si_3N_4 Structure," *J. Mater. Sci. Lett.*, **14**, 1749–51 (1979).

[7]K. H. Jack, "The Characterization of α′-SiAlON and the α–β relationships in SiAlON and Silicon Nitrides"; pp. 45–60 in *Progress in Nitrogen Ceramics*. Edited by F. L. Riley. Martinus Nijhoff, The Hague, Netherlands, 1983.

[8]S. Hampshire, K. P. J. O'Reilly, M. Leigh, and M. Redington, "Formation of α′-SiAlONs with Neodymium and Samarium Modifying Cations"; pp. 933–40 in *High Tech Ceramics*. Edited by P. Vincenzini. Elsevier Science Publishers B. V., Amsterdam, Netherlands, 1983.

[9]T. Ekstrom and M. Nygren, "SiAlON Ceramics," *J. Am. Ceram. Soc.*, **75** [2] 259–76 (1992).

[10]G. Z. Cao and R. Metselaar, "α′-SiAlON Ceramics: A Review," *Chem. Mater.*, **3**, 242–52 (1991).

[11]S. Wada and Y. Ukyo, "Microstructure and Properties of α/β-SiAlON Composites"; pp. 29–33 in *Proceedings of 34th Japan Congress on Materials Research*. The Society of Materials Science of Japan, Kyoto, Japan, 1991.

[12]S. Y. Liu, I-W. Chen, and T.-Y. Tien, "Fatigue Crack Growth of Silicon Nitride at 1400°C—A Novel Fatigue Induced Crack-Tip Bridging Phenomenon," *J. Am. Ceram. Soc.*, **77** [1] 165–71 (1994).

[13]S.-L. Hwang and I-W. Chen, "Reaction Hot-Pressing of Sialon Ceramics," *J. Am. Ceram. Soc.*, in review.

[14]D. Hardie and K. H. Jack, "Crystal Structures of Silicon Nitride," *Nature (London)*, **180**, 332–33 (1957).

[15]S. N. Ruddlesden and P. Popper, "On the Crystal Structures of the Nitrides of Silicon and Germanium," *Acta Crystallogr.*, **11**, 465–68 (1958).

[16]P. R. Marchand, Y. Laurent, and J. Lang, "Structure du Nitrure de Silicium α," *Acta Crystallogr.*, **B25**, 2157–60 (1969).

[17]K. L. More, "Defect Characterization in a CVD α-Si_3N_4"; pp. 936–37 in *Proceedings of the 49th Annual Meeting of the Electron Microscopy Society of America*. Edited by W. Bailey. San Francisco Press, San Francisco, CA, 1991.

[18]E. Butler, "Observations of Dislocations in β-silicon Nitride," *Philos. Mag.*, **21**, 829–33 (1971).

[19]A. G. Evans and J. V. Sharp, "Microstructural Studies on Silicon Nitride," *J. Mater. Sci.*, **6**, 1292–302 (1971).

[20]A. G. Evans and J. V. Sharp, "Transmission Electron Microscopy of Silicon Nitride"; pp. 1141–53 in *Electron Microscopy and Structure of Materials*. Edited by G. Thomas, R. M. Fulrath, and R. M. Fisher. California Press, Berkeley, CA, 1972.

[21]R. Kossowsky, "The Microstructure of Hot-Pressed Silicon Nitride," *J. Mater. Sci.*, **8**, 1603–15 (1973).

[22]W. E. William and G. E. Hilmas, "Microstructural Changes in β-silicon Nitride Grains upon Crystallizing the Grain Boundary Glass," *J. Am. Ceram. Soc.*, **72** [10] 1931–37 (1989).

[23]R. A. Youngman and T. G. Mitchell, "Defect Aggregates in Neutron-Irradiated β-Si_3N_4," *Radiat. Eff.*, **74**, 267–78 (1983).

[24]S.-L. Hwang, "Fabrication, Microstructural Characterization, and Deformation of Superplastic SiAlON Ceramic"; Ph.D. Dissertation. University of Michigan, Ann Arbor, MI, 1992.

[25]I-W. Chen and L. A. Xue, "Development of Superplastic Structural Ceramics," *J. Am. Ceram. Soc.*, **74** [4] 842–45 (1991).

[26]P. B. Hirsch, A. Howie, R. B. Nicholson, D. W. Pashley, and M. J. Whelan, *Electron Microscopy of Thin Crystals*. Kreiger, New York, 1977.

[27]H. Saka, "Burgers Vector Determination of Dislocations in an Elastically Anisotropic Crystal by High-order Reflection Imaging Techniques in an HVEM," *Philos. Mag. A*, **49**, 327 (1984).

[28]W. Y. Sun, T.-Y. Tien and T.-S. Yen, "Solubility Limits of α′-SiAlON Solid Solutions in the System Si,Al,Y/N,O," *J. Am. Ceram. Soc.*, **74** [10] 2547–50 (1991).

[29]J. V. Sharp, A. G. Evans, and B. Hudson, "Electron Diffraction Data for Silicon Nitride," Harwell Research Report AERE-R7319. Atomic Energy Research Establishment, Harwell, U.K., 1972.

[30]O. V. Biest and G. Thomas, "Identification of Enantiomorphism in Crystals by Electron Microscopy," *Acta Crystallogr.*, **A31**, 70–76 (1975).

[31]S. Serneels, M. Snykers, P. Delavignette, R. Gevers, and S. Amelinckx, "Fridel's Law in Electron Diffraction as Applied to the Studies of Domain Structures in Non-Centrosymmetrical Crystal," *Phys. Status Solidi B*, **58**, 277 (1973).

[32]R. Gever, P. Dilavignette, H. Blank, and S. Amlinckx, "Electron Microscope Transmission Image of Coherent Domain Boundaries," *Phys. Status Solidi*, **4**, 383 (1964).

[33]C. Chetfield, T. Ekström, and M. Mikus, "Microstructural Investigation of Alpha-Beta Yttrium SiAlON Materials," *J. Mater. Sci.*, **21**, 2297–307 (1986). □